

# Highly Improved Acetone Gas Sensing Performance of Mesoporous Cobaltic Oxide Nanoparticles and Physical Mechanism

[1] Madiha Khan<sup>1 a,b</sup>, [2] Ahtisham Anjum<sup>2c</sup>, [3] Muhammad Zaka<sup>3d</sup>,

[4] Irum Munir<sup>3d</sup>

[a] Department of Physics, Air University Islamabad, Pakistan, [b] Department of ingenieria, University of Messina, Itlay, [c] Department of Physics, King Fahad University of Petroleum & Minerals, Dhahran, 31261 KSA, [d] National institute of vacuum science and technology, National center of Physics, Islamabad, Pk

[1] madihakhan7121992@gmail.com,

[2] g202115850@kfupm.edu.sa, [3] zakaphy@gmail.com,

[4] irumm@ncp.edu.pk

**Abstract**— Mesoporous Cobaltic oxide nanoparticles are now widely employed in a variety of applications across the world. It is both environmentally and economically favorable. It was well prepared in this study using a cost-effective thermal stirring procedure. The X-ray diffraction method at ambient temperature was used to explain the formation of single spinel structure, purity, and cat-ion distribution of the material, and the lattice constant of mesoporous Cobaltic oxide nanoparticles was 8.23 Å. SEM and EDX examination were used to investigate phase formation, elemental content, and surface morphology. The average particle size for primitive mesoporous Cobaltic oxide nanoparticles is 17nm. DRS determined the band gap for mesoporous Cobaltic oxide nanoparticles to be 1.48 eV for direct band bending and 2.19 eV for indirect band gap. The sensitivities of the sample are greater due to the mesoporous-structures with a large surface area. Mesoporous Cobaltic oxide nanoparticles have a greater specific surface area ( $59.63\text{m}^2\text{g}^{-1}$ ), resulting in good acetone gas sensing characteristics at the optimal working temperature of 150°C. Furthermore, the sample exhibits high stability and selectivity against acetone gas. The gas-sensing mechanism is determined by comparing the sensitivity of Mesoporous Cobaltic oxide nanoparticles to surface oxygen and acetone gas adsorption. It is the best among the top other materials, according to the results.

**Index Terms**— Cobaltic oxide, gas sensing device, material morphology, nanoparticles, physical properties.

## I. INTRODUCTION

Acetone is a popular solvent used in the production of plastics and other industrial goods. Acetone can also be found in a limited number of domestic items, such as cosmetics and personal care products, where it is most employed in the formulation of nail polish removers [1]. Acetone, a flammable, dangerous, and combustible gas, has an anesthetic effect on the central nervous system at concentrations more than 0.0211 ppm according to international standards, and has been identified by the International Cancer Research Center as a very hazardous carcinogen. As a result, detecting and monitoring acetone gas in real time is extremely critical [2]. Until date, the primary detection approach for acetone gas has been instrument analysis (such as gas chromatography), which is incapable of monitoring in real time or short-term detection. Various gas sensors, such as resistive gas sensors, quartz crystal microbalance gas sensors, surface acoustic wave gas sensors, and organic thin film transistor gas sensors, are now utilized to detect and monitor hazardous, flammable, and explosive gases [3-7]. Semiconductor metal oxide (SMO) gas sensors are the best for detecting acetone gas because of their inexpensive cost, low power consumption, great selectivity, and long-term stability [8-11]. The gas-sensing performance of SMO sensors is determined by the change in resistance generated by oxygen and target gas adsorption on the surface of the SMO. SMO are classified into two categories based on the type of conducting carrier: n-type ( $\text{SnO}_2$  [12,13],  $\text{ZnO}$  [14,15],  $\text{In}_2\text{O}_3$  [16,17],  $\text{WO}_3$  [18,19], and  $\text{Fe}_2\text{O}_3$  [20,21]) and p-type ( $\text{CuO}$  [22,23],  $\text{Co}_3\text{O}_4$  [24,25],  $\text{NiO}$  [26, 27] and  $\text{Cr}_2\text{O}_3$  [27]). In comparison to the more well-studied n-type SMO sensors, the p-type SMO sensors have a better catalytic action, particularly with acetone, and are less reliant on humidity, resulting in improved stability. Because research on p-type SMO sensors is insufficient, the matching p-type SMO sensors that work well on volatile organic chemicals are more common now [28].

$\text{Co}_3\text{O}_4$  is a substantial anti-ferromagnetic p-type semi-conductor transition metal-oxide with direct bandgaps of 1.48 and 2.19 eV [1-5]. Cobalt oxide exists in three forms:  $\text{CoO}$ ,  $\text{Co}_2\text{O}_3$ , and  $\text{Co}_3\text{O}_4$ . It is a naturally abundant and environmentally beneficial substance [6] with high redox activity. Cobalt oxide is a less expensive material than other transition metal oxides. Primal  $\text{Co}_3\text{O}_4$  has numerous applications, one of which is the detection of ethanol [7, 8]. Non-stoichiometry has a key effect in modifying the number of adsorbed oxygen types and gas sensing characteristics in Primal Cobaltic oxide ( $\text{Co}_3\text{O}_4$ ) [9]. Because of its excellent oxidative catalytic reactivity, sufficient conductivity, higher charge capacity, significant chemical stability, and simplified electronic transportation between  $\text{Co}^{2+}$  and  $\text{Co}^{3+}$  ions, Nano primal cobaltic oxide ( $\text{Co}_3\text{O}_4$ ) has attracted considerable interest as an active material, particularly in electrochromic tools, heterogeneous catalysis, magnets, super capacitors, Li-ion batteries, and gas sensors [1,10].

$\text{Co}_3\text{O}_4$  nanostructures have been extensively researched as gas-sensing media for detecting hazardous and explosive gases. Until now, the following steps have been used to improve the gas-sensing performance of  $\text{Co}_3\text{O}_4$  sensors: (1) controlling the morphology and microstructures of  $\text{Co}_3\text{O}_4$  nanostructures to increase surface area; (2) doping metal atoms to change the carrier concentration; and (3) forming nanocomposites with heterojunctions to adjust the interfacial carrier concentrations [35]. Cao et al. found that the porous-structure

Co<sub>3</sub>O<sub>4</sub> gas sensor could detect benzene, toluene, and xylene gases swiftly and selectively [36]. Zhang et al. created mesoporous Sn-doped Co<sub>3</sub>O<sub>4</sub> whiskers, which demonstrated a high sensitivity to toluene gas [37].

Controlling the microstructure and morphology is the most fundamental and significant technique to increase surface area and change surface gas adsorption in Co<sub>3</sub>O<sub>4</sub> nanostructures to improve gas-sensing performance [38]. So far, various techniques have been developed for the manufacture of Primal Cobaltic oxide (Co<sub>3</sub>O<sub>4</sub>) nanostructures such as nanospheres, nanotubes, nanocubes, nanoflowers, nanofibers, nanosheets, nanorods, hollow microspheres, and core-shell structures for gas sensing applications [11-18].

Cao et al. used a moderate hydrothermal technique to manufacture Co<sub>3</sub>O<sub>4</sub> hollow nanosheets, and the as-prepared Co<sub>3</sub>O<sub>4</sub> sensor demonstrated high selectivity, quick response-recovery speed (1 s and 9 s), and stable repeatability to toluene gas [44]. Teng et al. used carbonaceous templates to create hollow Co<sub>3</sub>O<sub>4</sub> microspheres that were more sensitive to CO than pure Co<sub>3</sub>O<sub>4</sub> nanoparticles [45]. Geng et al. produced Co<sub>3</sub>O<sub>4</sub> nano-octahedral structure using a simple and innovative coordination compound precursor method, which demonstrated good CO and CH<sub>4</sub> sensitivity at ambient temperature [46]. Xu et al. used a simple hydrothermal process to create a well-arranged array of Co<sub>3</sub>O<sub>4</sub> nanowires with an excellent reaction to 100 ppm triethylamine gas [47].

As previously demonstrated, increasing the surface area of nanostructures can increase their gas-sensing ability [25,48,49]. Thermal stirring was used to create Mesoporous Cobaltic oxide nanoparticles to investigate the effect of microstructures and shape on gas-sensing capability. Subsequently. Only in this manner could the impact of Mesoporous Cobaltic oxide nanoparticles' microstructures and shape on gas-sensing capability be exposed in depth. Finally, based on surface oxygen and acetone gas adsorption, the gas-sensing method Mesoporous Cobaltic oxide nanoparticles for acetone gas was determined.

## II. EXPERIMENTAL DETAILS

### A. Preparation of primal Cobaltic oxide (Co<sub>3</sub>O<sub>4</sub>)

Cobalt nitrate was bought commercially from Aldrich scientific store Co (NO<sub>3</sub>)<sub>2</sub>.6H<sub>2</sub>O (98 wt.% Synth), and cobalt oxide nanoparticles were produced using the co-precipitation technique. As a precursor, cobalt nitrate Co (NO<sub>3</sub>)<sub>2</sub>.6H<sub>2</sub>O, sodium hydroxide (NaOH), and deionized water were used to make Co<sub>3</sub>O<sub>4</sub>. To begin, nitrate was dissolved in dionized water according to stoichiometry, and 5M of NaOH solution was dissolved in deionized water. The combined NaOH solution was then dropped into the nitrate's solution. The pH of precipitates was kept constant at 12 while the temperature was kept constant at 60 °C. Following the production of precipitates, the solution was agitated for another 5 hours, heated under vigorous stirring (about 250 °C), and rinsed multiple times with deionized water. The precipitates were then removed from the solution by centrifugation and dried in a vacuum oven at 80 °C for 2 hours.

To create crystalline  $\text{Co}_3\text{O}_4$  nanoparticles, the powder was ground and calcined in the furnace at  $500^\circ\text{C}$  for 3 hours under ambient circumstances. The powder is now ready for analysis. The flow diagram of synthesis particles is depicted in Figure-2.1.

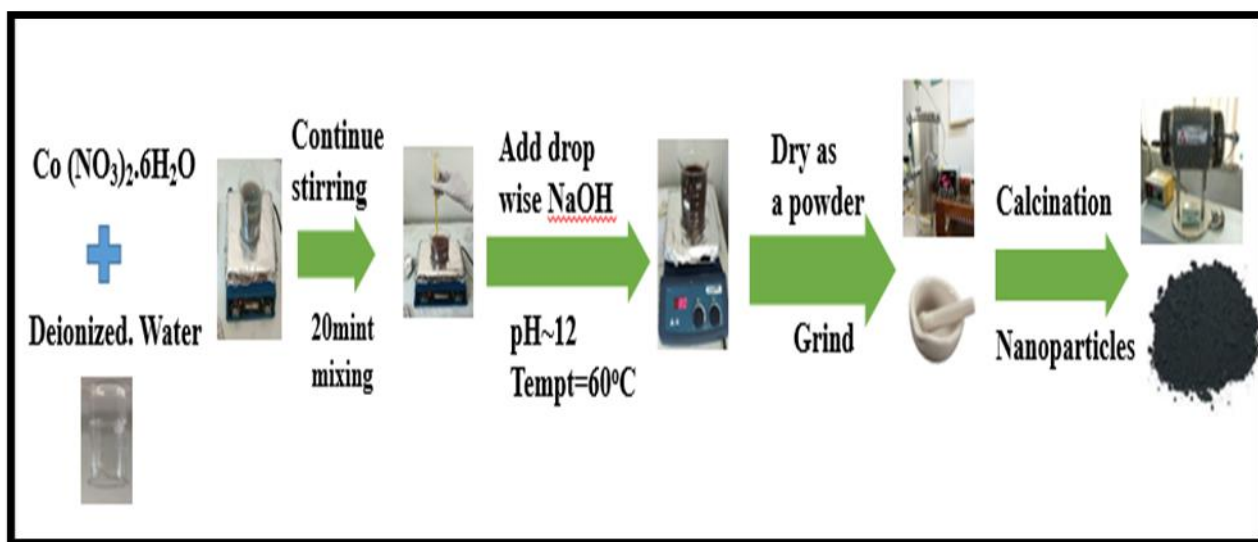


**Fig.1. Mesoporous Cobaltic Oxide Nanoparticle Synthesis.**

### III. CHARACTERIZATION

XRD (SmartLabSE (3 kW), Cu target, wavelength 0.154 nm, step  $0.02^\circ$ ), and TEM were used to analyse the crystal structure and morphology of Mesoporous Cobaltic oxide nanoparticles (JME-1200EX). To determine the bandgap and specific surface area of Mesoporous Cobaltic oxide nanoparticles, the DRS spectra and nitrogen adsorption-desorption isotherms were determined at  $150^\circ\text{C}$  using a UV3600 spectrophotometer and a Micrometrics ASAP 2020 surface area and porosity analyzer. The Current-Voltage (I-V) approach was used to do the conductivity analysis. At room temperature, magnetic characteristics were measured using a vibrating sample magnetometer (Lakeshore, model 7404). (RT). Finally, static distribution on a resistive gas-sensing measuring system was used to perform gas-sensing experiments with ambient air as the interference gas.

### IV. SENSOR FABRICATION

The design and construction of a gas sensor are both critical components. Many factors must be made while building a gas sensor, including the specificity of the sensor and its level of sensitivity to a certain gas. Metal oxide gas sensors may be made using a variety of techniques. Other factors to consider are the cost of the manufacturing procedure, porosity, the purity of the sensing material, and dependability. If the price is too high, the demand for it will be reduced. The same is true for materials; more porosity indicates more adsorption sites and, thus, higher sensitivity. To assess the electrical properties, the sensing layer is usually put on top of a thin film substrate or a thick film substrate that already has electrodes.

A solid-state gas sensor device is typically made up of a sensing element layer placed on a patterned ceramic substrate. Material was deposited using the drop-casting process. Thick

films are straightforward to deposit using relatively inexpensive procedures based on the thickness of the sensing element (thickness more than 1  $\mu\text{m}$ ). To make a thick film, dissolve 0.1 mg of powder material in  $\mu\text{l}$  deionized water first. The solution should then be sonicated until the particles are completely dispersed in the water. After placing the solution in the sensing device, allow it to dry at ambient temperature. It should be noted that the sensing material completely covers the sensing element. A thick, homogenous layer is formed.

To complete the circuit, gently insert the sensor element into the holder. Place it in the sensing chamber. The electrical current passing through the sensing element is a function of the partial pressure of the target gas in the surrounding environment and the operating temperature when a fixed voltage is applied. The change in electrical resistance caused by a change in target gas concentration indicates the sensor's output, as shown in Figure-2.2.

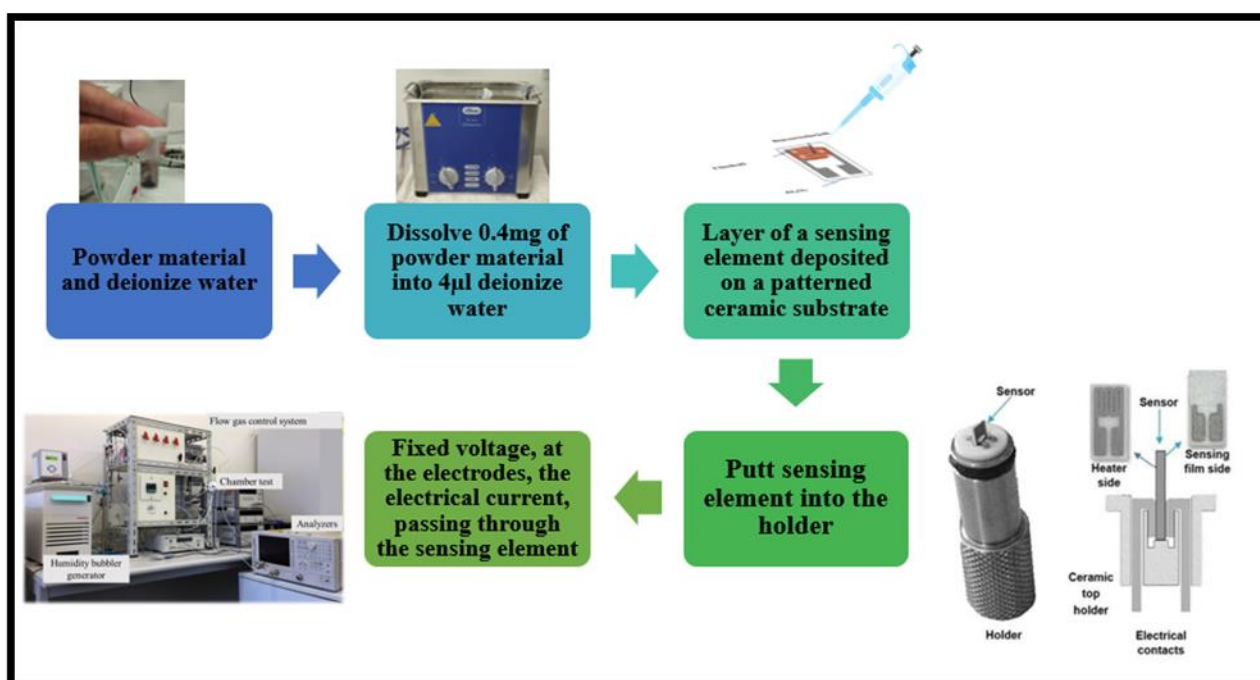


**Fig.2. The Fabrication of resistive gas sensors by drop casting technique.**

## V. RESULTS AND DISCUSSION

### A. X-rays Diffraction Analysis (XRD)

Figure-3.1 depicts the X-ray diffraction patterns of the produced materials, namely primitive Cobaltosic oxide ( $\text{Co}_3\text{O}_4$ ) at room temperature (a). To establish phase formation, the produced sample's XRD pattern is compared to the XRD patterns of conventional primordial Cobaltosic oxide ( $\text{Co}_3\text{O}_4$ ), JCPDS card no. 74-2120. As a result of the comparison, it is discovered that the produced sample of  $\text{Co}_3\text{O}_4$  in face centred cubic (FCC) spinel structure with the  $Fd3m$  space group is superior. Furthermore, there are no un-matched peaks in the XRD pattern, indicating that the manufactured samples are exceedingly pure and crystalline in nature. The average crystallite size of our prepared sample was calculated using Scherer's method from the greatest exciting peak (311), see eq. (3.1).

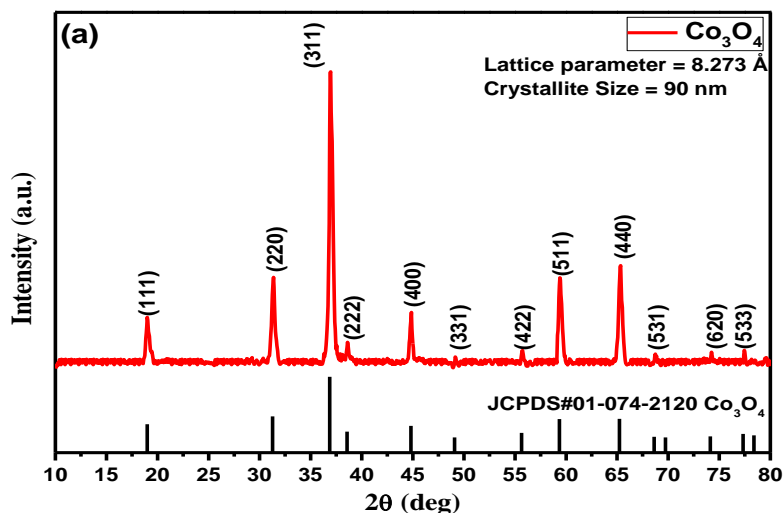


**Fig-3. Mesoporous Cobaltic oxide nanoparticle X-ray diffraction spectrum.**

$$D = 0.9 \frac{\lambda}{\beta \cos\theta} \dots \dots \dots (3.1)$$

Where, D is the average size of crystallite, k is the machine constant (k = 0.9), λ is the wavelength of the CuKα (1.5418 Å) and β is the diffraction peaks broadening (calculated at half maximum intensity).

**TABLE 1. MESOPOROUS COBALTOSIC OXIDE NANOPARTICLES' MICRO STRAIN, LATTICE**

Sampl e	Micro Strain	Lattice Constant (Å)	Cell Volume V(A) <sup>3</sup>	Density (g/cm <sup>3</sup> )	Porosity %	Crystallite Size (nm)
Co <sub>3</sub> O <sub>4</sub>	0.00145	593.49	566.24	4.906	0.241	90.00

CONSTANT, CELL VOLUME, POROSITY, AND CRYSTALLITE SIZE.

**Table 2. XRD Analysis of Mesoporous Cobaltic oxide nanoparticles.**

Sample	Position 2thete [°]	Highest [cts]	FWHM [°]	d-spacing [Å]	Crystallite Size (nm)
Co <sub>3</sub> O <sub>4</sub>	36.89	365.81	0.0984	2.434	90.00

*B. SEM and EDX analysis*

SEM images of Mesoporous Cobaltic oxide nanoparticles are shown in Figure-3.2(a). The particles have the appearance of Nano spheres. The particle size varied from 5 to 30 nm. The nanosphere particles clump together and create a microsphere. The rise in particle size from nanometer to micrometre in relation to the change in morphology demonstrates that the

precursor amount influences the surface morphology of the manufactured product. The EDX spectra clearly showed the elemental composition of Mesoporous Cobaltosic oxide nanoparticles (Figure-3.2(b)). The strong and intense peaks of Co and Oxygen (O) atoms indicated the presence of impurity-free Mesoporous Cobaltosic oxide nanoparticles. The Cu/Cr electrode is to blame; the additional Na and C peaks in the spectrum were caused by Cu/Cr electrodes. It is widely known that the windowless EDX analyzer can identify elements ranging from boron (atomic number 5) to the principal elements found in tissues (carbon, nitrogen and oxygen). The elemental composition is stated in Table.3.

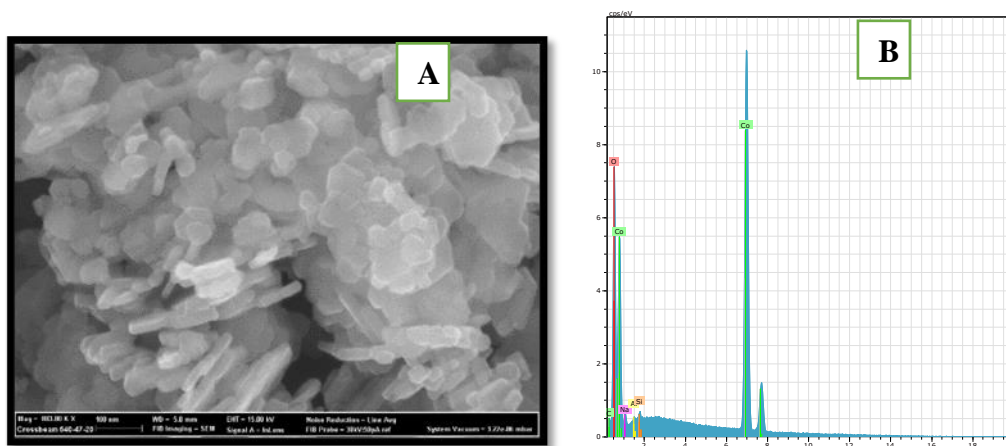


**Fig.4. (a) Nanostructures Mesoporous Cobaltosic oxide nanoparticles.**

**Prepared by thermal stirring method and (b) its elemental composition.**

**Table 3. EDX elemental composition of Mesoporous Cobaltosic oxide nanoparticles.**

Sample	Element	Wt.%	Atom%
Co <sub>3</sub> O <sub>4</sub>	O,Co,C,Na,Si, and Al	31.77, 59.30,5.60,2.11, 0.67, and 0.56	55.24, 27.99, 12.98,2.55,0.66, and 0.58

### *C. Diffuse Reflectance Spectroscopy analysis*

The most frequent approach for ensuring nanoparticle production is DRS spectral analysis. Figure 3.3 depicts the band gap spectra of Mesoporous Cobaltosic oxide nanoparticles (a).

The Mesoporous Cobaltosic oxide nanoparticles have a bandgap peak at 1.48 (units) for direct band bending and 2.19 eV for indirect band bending. The -metal charge transfer is shown by the prominent peak in the DRS region. When compared to other previously published studies in the same subject area, the current study's findings are superior. The strong peak is attributed to electron-hole radiative recombination. Furthermore, when particle size decreases, the bandgap energy increases and the transmission peak changes to shorter wavelengths.

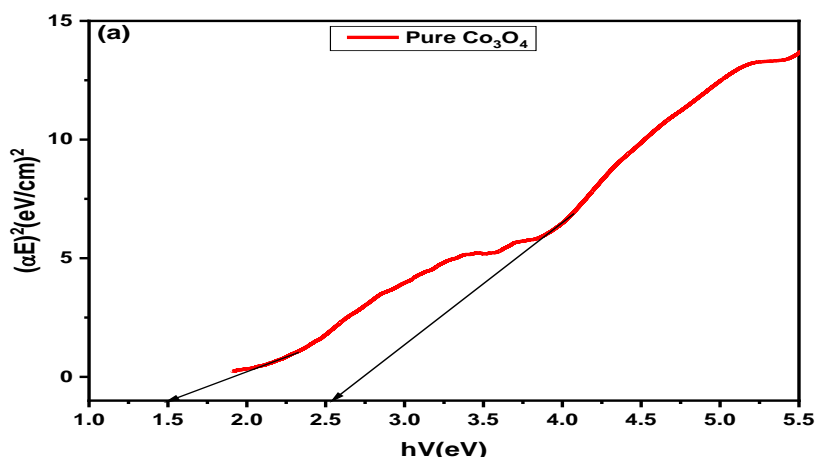


**Fig.5. DRS spectra of Mesoporous Cobaltic oxide nanoparticles**

**Table 3. DRS analysis for the pure Co<sub>3</sub>O<sub>4</sub> nanoparticles**

Sample	Phase	Space group	Band gap [eV]	Type of band gap	Crystal Structure
Co <sub>3</sub> O <sub>4</sub>	Single	Fd3m	1.48 and 2.19	Direct and indirect	Cubic

*D. BET results.*

The outstanding gas sensor performance in our study is thought to be due to the extraordinary unique structure of Mesoporous Cobaltic oxide nanoparticles with a beneficial characteristic. Brunauer-Emmett-Teller gas-sorption measurements were carried out to study the specific surface area and pore-size distribution of the produced Mesoporous Cobaltic oxide nanoparticles.

The BET surface area of Co<sub>3</sub>O<sub>4</sub> was approximately 59.63 m<sup>2</sup> g<sup>-1</sup>, as shown in Fig 3.8. Table 3.8 and the insets of Figures 3.8(a,b). The majority of pores were around 3.7 nm in diameter, with an average diameter of 6.8 nm. The greater surface area of Co<sub>3</sub>O<sub>4</sub> is attributable to the acquired porous structure following calcination when compared to the BET surface area with prior results. Co<sub>3</sub>O<sub>4</sub> Nano powder's high surface area and empty spaces enable more active interaction sites between gas and active materials, which are responsible for the quick and high response.

**Table 4 BET Analysis of pure Co<sub>3</sub>O<sub>4</sub> nanoparticles**

Sample	Surface area (m <sup>2</sup> g <sup>-1</sup> )	Pore Volume (cc/g)	Pore radius(Å)
Co <sub>3</sub> O <sub>4</sub>	59.634	8.403 0.102	8.403 990.493

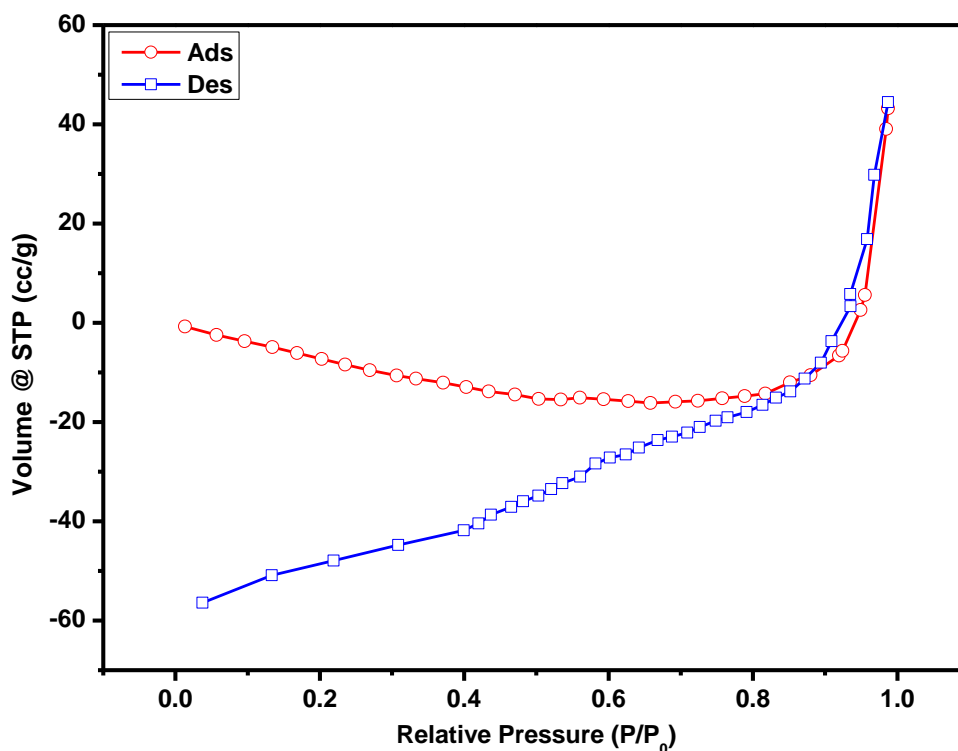


**Fig.6. BET results of Mesoporous Cobaltosic oxide nanoparticles (Isotherm: Log Scale)**

#### *E. Vibrating Sample Magnetometry (VSM)*

All samples were magnetically measured at room temperature using a Vibrating Sample Magnetometer (VSM) with a magnetic field of up to 20 kOe. Figure 1 depicts the magnetic properties of prepared Mesoporous Cobaltosic oxide nanoparticles. 3.4.

VSM patterns of pure sample Mesoporous Cobaltosic oxide nanoparticles show ferromagnetic activity, with a saturation magnetization ( $M_S$ ) of around 8.50 (emu/g) and a coercive field ( $H_c$ ) of about 85.01 (Oe).

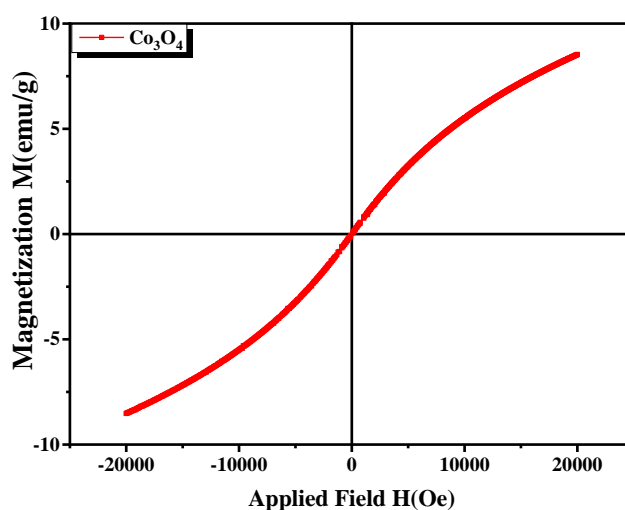


**Fig.7. VSM spectra of Mesoporous Cobaltosic oxide nanoparticles**

**Table 5. Magnetic characteristics of Cobaltosic oxide (Co<sub>3</sub>O<sub>4</sub>) nanoparticles at room temperature.**

Sample	H <sub>c</sub> (Oe)	M <sub>s</sub> (emu/g)	M <sub>r</sub> (emu/g)	M <sub>r</sub> / M <sub>s</sub>
Co <sub>3</sub> O <sub>4</sub>	85.01	8.50	0.70973	0.2908

*F. Fourier Transform Infrared (FTIR)*

The functional groups contained in the Mesoporous Cobaltosic oxide nanoparticles were confirmed using FTIR studies. Figure 3.4 depicts the FTIR spectra of Mesoporous Cobaltosic oxide nanoparticles (a).

In the examined region (4000–500 cm<sup>-1</sup>), absorption peaks around 3787 cm<sup>-1</sup>, 14356 cm<sup>-1</sup>, 840 cm<sup>-1</sup>, 668 cm<sup>-1</sup>, and 556 cm<sup>-1</sup> are observed. The absorption bands at 851 cm<sup>-1</sup> and 644.79 cm<sup>-1</sup>, originating from the metal-oxygen bond (Co-O), it happened during the stretching vibrations. It also confirms the formation of Mesoporous Cobaltosic oxide nanoparticles.

In addition, the broad band centered at 3386 cm<sup>-1</sup> and the peak at 1633 cm<sup>-1</sup> are respectively assigned to O-H stretching and bending vibration modes of absorbed water molecules. Peaks at 1387 cm<sup>-1</sup> and 1105 cm<sup>-1</sup> are assigned to Co-O-H vibrations. In the FTIR spectrum, all of the peaks verified the development of Mesoporous Cobaltosic oxide nanoparticles. Metal oxygen frequencies are below requirements for the relevant metal oxides when compared to published values.

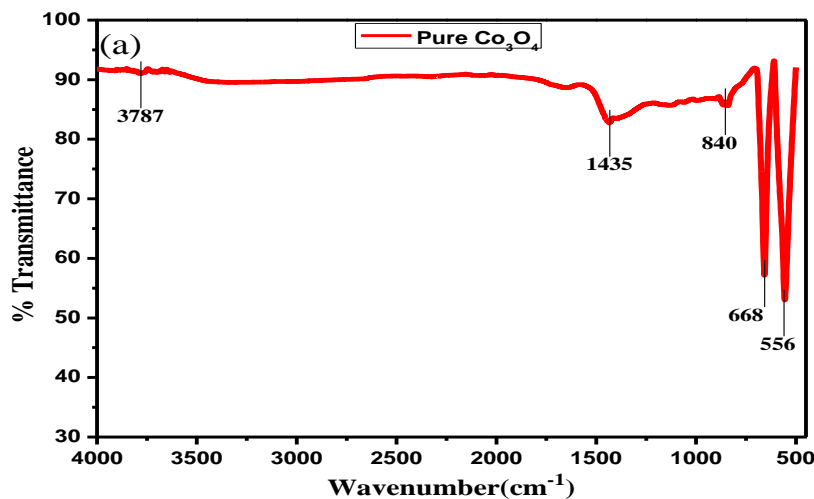


**Fig.8. FTIR spectra of Mesoporous Cobaltosic oxide nanoparticles**

*G. I-V (Current Voltage) characteristics*

Figure-3.4(a) depicts typical room temperature current-voltage (I-V) characteristics of the films in the bias range of -1 to +1 V due to the presence of many vacancies and defect sites. Hysteretic nature is a common factor observed in oxide materials due to the presence of many vacancies and defect sites. The entrapment of charge carriers causes this hysterical behavior. In this situation, the straight I-V characteristics flowing through the origin indicate the Ohmic contact between the silver paste and the Mesoporous Cobaltosic oxide nanoparticles thin film.

Exotically, I-V curves for samples are straight and non-hysteretic. Linear I-V uniqueness is discovered, which might be attributed to strong grain-to-grain communication. The I-V characteristics reveal that there is a reduction in resistance obtained for the sake of grain size. Increased grain size leads to increased electron mobility.

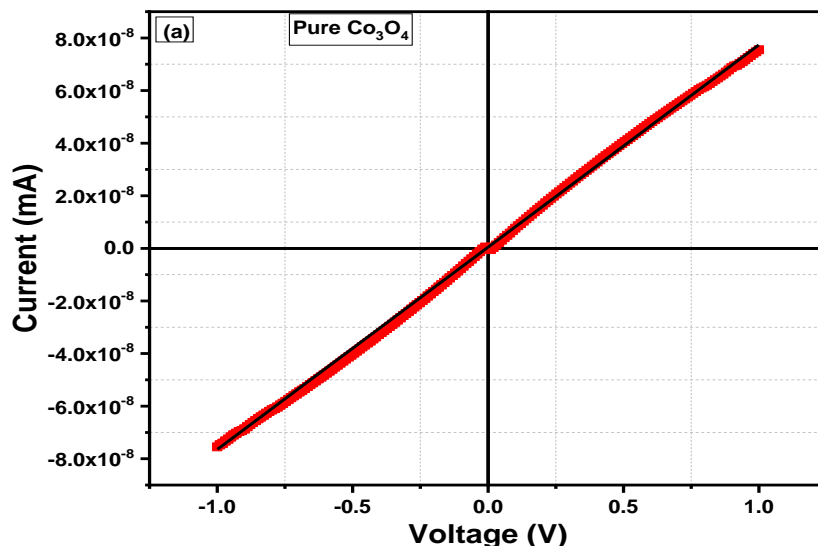


**Fig.9. I-V images of Mesoporous Cobaltosic oxide nanoparticles**

#### *H. Raman Spectroscopy of Mesoporous Cobaltosic oxide nanoparticles*

The Raman spectra of the produced Mesoporous Cobaltosic oxide nanoparticles at room temperature is given in Fig 3.6. The Raman spectrum of Mesoporous Cobaltosic oxide nanoparticles, shown in fig 3.7, has ten distinct peaks at roughly 192, 267, 408, 476, 515, 613, and 682  $\text{cm}^{-1}$  corresponding to Mesoporous Cobaltosic oxide nanoparticles. The peaks at 192, 408, 515, 613, and 682  $\text{cm}^{-1}$  correspond to the five Raman-active modes of Mesoporous Cobaltosic oxide nanoparticles, and the results are compatible with the Raman spectra of crystalline Mesoporous Cobaltosic oxide nanoparticles described before.

The Raman mode at 679  $\text{cm}^{-1}$  is associated with octahedral vibrations, whilst the other modes are associated with tetrahedral and octahedral coupled vibrations, respectively. However, cobalt caused a maximum shift of roughly 20 towards higher wavenumber for several peaks, which can be attributed to size effects or surface stress/strain.

Chemical reactions and toluene gas transport at the surface of Mesoporous Cobaltosic oxide nanoparticles have a significant impact on the process of oxygen and acetone gas adsorption and desorption [56]. Acetone gas cannot be heated sufficiently to react with the oxygen ions absorbed on the surface of Mesoporous Cobaltosic oxide nanoparticles, resulting in limited sensor response at low temperatures. When the temperature rises sufficiently, the thermal energy of toluene becomes too high to absorb on the surface and react with oxygen ions, and the toluene reaction diminishes to some amount.

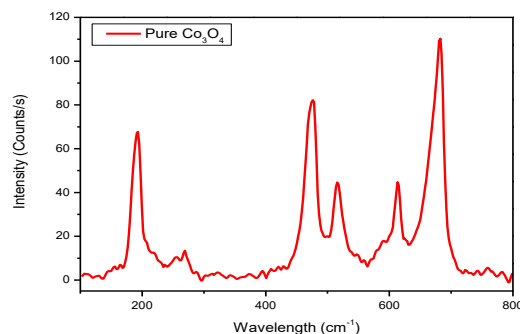


**Fig.10. Raman spectra of Mesoporous Cobaltosic oxide nanoparticles**

### *I. Gas Sensing Properties*

Mesoporous Cobaltosic oxide nanoparticles' gas-sensing performance is investigated as follows:

To begin, the responses of Mesoporous Cobaltosic oxide nanoparticles gas sensors were evaluated at temperatures ranging from 50 to 300°C in 40 ppm acetone gas to validate the ideal working temperature shown in Fig. 3.7 (a) (a). Mesoporous Cobaltosic oxide nanoparticle sensitivities rise fast with increasing operation temperature, peaking at 150°C and subsequently decreasing to some extent. The rate of chemical reactions and acetone gas diffusion at the surface Mesoporous Cobaltosic oxide nanoparticles have a significant impact on the process of oxygen and acetone gas adsorption and desorption [56]. Acetone gas cannot be heated sufficiently to react with the oxygen ions absorbed on the surface of Mesoporous Cobaltosic oxide nanoparticles, resulting in limited sensor response at low temperatures. When the temperature rises sufficiently, the thermal energy of acetone becomes too great to absorb on the surface and react with oxygen ions, and the acetone reaction reduces to some amount. As a result, when the thermal energy of acetone gas and activation energy match, the best operating temperature is proven to be 150°C.

Following the determination of the sensor's optimal operating temperature, the resistance of the sensor in air with temperatures less than 150°C was examined. The resistance transients of the Mesoporous Cobaltosic oxide nanoparticles sensors to varied temperatures below 150°C in air are shown in Figures-3.7(b). Mesoporous Cobaltosic oxide nanoparticles sensors demonstrated greater resistance, as shown in Figure-3.7(b), which might be attributed to the higher inherent resistance of Mesoporous Cobaltosic oxide nanoparticles sensors.

The Mesoporous Cobaltosic oxide nanoparticles sensors demonstrated better resistance to acetone gas, which might be attributed to their higher intrinsic resistance. The sensing device's resistance decreased after being exposed to acetone gas. It is also noted that after each pulse, the signal returns to its initial baseline value. This finding demonstrates that acetone adsorption on the surface layer is completely reversible. The calibration curve of Mesoporous Cobaltosic oxide nanoparticles sensors at 150°C is shown in Figure-3.7(c). The Mesoporous Cobaltosic oxide nanoparticles sensors were more sensitive to acetone gas at 10-80 ppm concentrations than the earlier pristine Co<sub>3</sub>O<sub>4</sub> sensors. It is also noted that after each pulse, the signal returns to

its initial baseline value. This finding demonstrates that acetone adsorption on the surface layer is completely reversible.

Fig. 1 shows the response and recovery curves of Mesoporous Cobaltic oxide nanoparticles sensors to 40 ppm acetone at 150°C. 3.7(d). The response and recovery periods are defined as the time necessary for a change in resistance to reach 90% of the equilibrium value following acetone gas injection and removal [57]. The response time of Mesoporous Cobaltic oxide nanoparticles sensors is 225sec, while the recovery time is quite lengthy, with a value of 250sec. At 150°C, the resistance value of the sample is around 104 in air and 105  $\Omega$  in 40ppm acetone gas, which may be utilized to manufacture acetone gas sensors in practice.

The responses of Mesoporous Cobaltic oxide nanoparticles sensors to acetone gas concentrations ranging from 10-80 ppm at 150°C are shown in Fig. Figure-3.7. (d). It can be shown that sensor responses increase with acetone gas concentrations ranging from 10 to 80 ppm. When the concentration of acetone gas exceeds 10 ppm, the growth tendency slows. Acetone gas with a larger concentration interacts with more absorbed oxygen, resulting in a significant change in resistance. The responses follow the order of Mesoporous Cobaltic oxide nanoparticles sensors  $> 1$  at the same concentration for the higher surface area of Mesoporous Cobaltic oxide nanoparticles sensors. In Table 2, the gas response of Mesoporous Cobaltic oxide nanoparticles sensors is substantially greater than that of previously reported Co<sub>3</sub>O<sub>4</sub>-based sensors.

Figure-3.7 depicts the reactions of a Mesoporous Cobaltic oxide nanoparticles sensor to 40ppm acetone, ammonia, ethanol, and formaldehyde gases at an operating temperature of 150°C. (e): Mesoporous Cobaltic oxide nanoparticles sensors respond best to acetone gas, then ethanol, formaldehyde, and ammonia. The sensitivity of Mesoporous Cobaltic oxide nanoparticles sensor to acetone gas is substantially higher than that of other Co<sub>3</sub>O<sub>4</sub> sensors, whereas the difference in sensitivity between Mesoporous Cobaltic oxide nanoparticles sensor and other gases is much smaller.

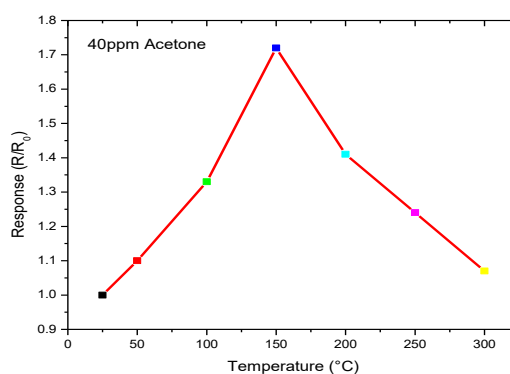


**Fig.11. Mesoporous Cobaltic oxide nanoparticles sensors' reactions to acetone gas (40ppm) at various operating temperatures**

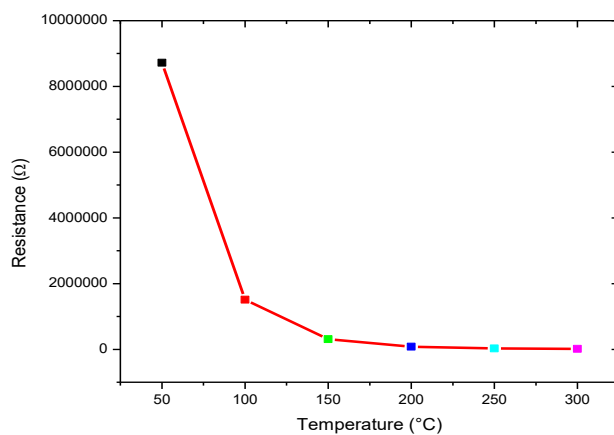


**Fig.12. Mesoporous Cobaltic oxide nanoparticles sensors' baseline resistance vs temperature spectrum**

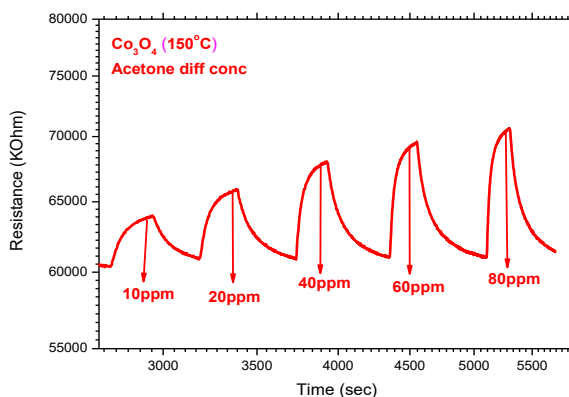


**Fig.13. Resistance vs. time of Mesoporous Cobaltic oxide nanoparticles sensors to acetone the reproducibility to acetone gas at varied concentrations and temperatures up to 150°C**

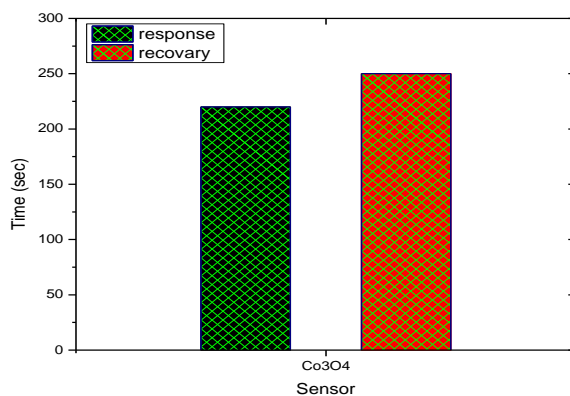


**Fig.14. The acetone gas repeatability of Mesoporous Cobaltic oxide nanoparticles sensors**

**Table 6. Gas response of various Co<sub>3</sub>O<sub>4</sub>-based sensors as reported in literature.**

Sensing material	T (° C)	Concentration (ppm)	Response	Reference
Mesostructure Co <sub>3</sub> O <sub>4</sub>	175	100 (ethanol)	7	43

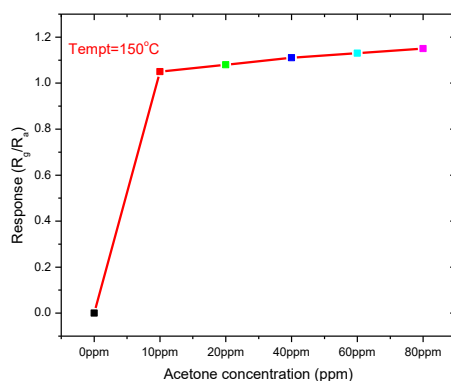


**Fig.15. The concentration-dependent response curves of Mesoporous Cobaltic oxide nanoparticles sensor responses at various concentrations**

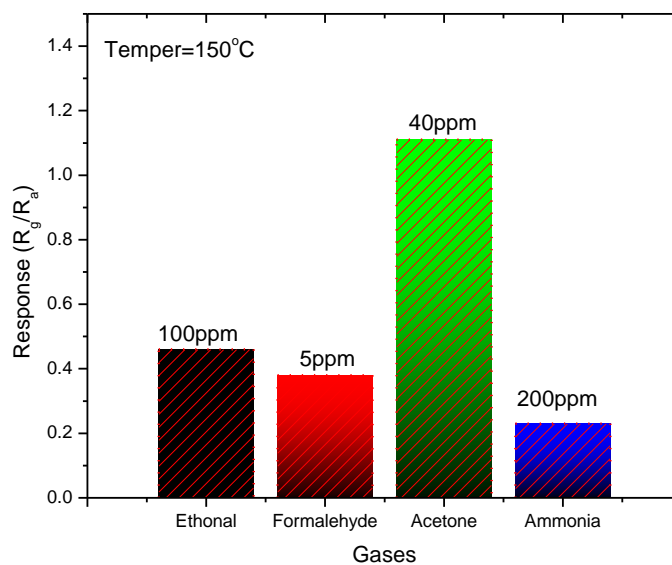
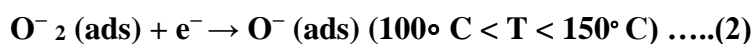


**Fig.16. The selectivity of Mesoporous Cobaltic oxide nanoparticles sensor at 150°C.**

### J. Sensing Mechanism

At different temperatures, the adsorbed oxygen on the surface of the Mesoporous Cobaltic oxide nanoparticles sensor absorbed the inner electrons to create anionic oxygen ( $O_2^-$ ,  $O^-$ ,  $O_2^{2-}$ ) according to the formula below [7]. Therefore, the hole accumulation layer on the surface of

the Mesoporous Cobaltosic oxide nanoparticles sensor formed. The resistance is therefore made up of particle resistance and core resistance. The resistance of the particles is considerably impacted by the adsorption of oxygen and acetone gas in this case, although the total resistances rarely change. The resistance of p-type SMO, as previously described [29], may be explained by the conflict between parallel circuits of shell area and core area.



## CONCLUSION

Thermal stirring was used to successfully produce Mesoporous Cobaltosic oxide nanoparticles. XRD, SEM, and EDX were used to determine the crystallinity, particle size, and morphology of Nano powders. DRS exhibited optical bands of 1.48 and 2.19 eV and 2.2 eV for Mesoporous Cobaltosic oxide nanoparticles samples. The presence of FTIR peaks verified the development of Mesoporous Cobaltosic oxide nanoparticles. The Ohmic behaviour of nanoaprticles was validated by the I-V characteristic curves. Mesoporous Cobaltosic oxide nanoparticles showed a modest hysteresis loop at ambient temperature. This might be explained by uncompensated surface spins or limited size effects. Both samples have better sensitivity than others and exhibit outstanding stability and selectivity to acetone gas. The surface area of Mesoporous Cobaltosic Oxide Nanoparticles is greater than that of Mesoporous Cobaltosic Oxide Nanoparticles ( $59.63\text{m}^2\text{g}^{-1}$ ). Therefore, Mesoporous Cobaltosic oxide nanoparticles have a greater sensitivity to acetone gas of 11.761. Given the sensitivity of Mesoporous Cobaltosic oxide nanoparticles, it was determined that the gas-sensing mechanism occurs from surface oxygen and toluene gas adsorption. As a result, in practice, the high-performance acetone gas sensor can be prepared with Mesoporous Cobaltosic oxide nanoparticles.

## REFERENCES

1. Wang, W. Tian, T. Zhai, C. Zhi, Y. Bando, and D. Golberg, *J. Mater. Chem.* 22, 23310 (2012)
2. W.-T. Koo, S. Yu, S.-J. Choi, J.-S. Jang, J. Y. Cheong, and I.-D. Kim, *ACS Appl. Mater. Interfaces* 9, 8201 (2017).
3. S. Bai, L. Du, J. Sun, R. Luo, D. Li, A. Chen, and C.-C. Liu, *RSC Adv.* 6, 60109 (2016).  
K.Deng, L. Wang, Z. Lou, and T. Zhang, *RSC Adv.* 4, 21115 (2014).
4. T. Liu, J. Liu, Q. Liu, Y. Sun, X. Jing, H. Zhang, and J. Wang, *Cryst Eng Comm* 18, 5728 (2016).
5. H. Wang, C. Li, P. Fang, Z. Zhang, and J. Z. Zhang, *Chem. Soc. Rev.* 47, 6101 (2018).
6. Amann, B. d L. Costello, W. Miekisch, J. Schubert, B. Buszewski, J. Pleil, N. Ratcliffe, and T. Risby, *J. Breath Res.* 8, 034001 (2014).
7. Kolodziejczak-Radzimska and T. Jesionowski, *Materials* 7, 2833 (2014).
8. S. Das and V. Jayaraman, *Prog. Mater. Sci.* 67, 161 (2015).
9. S. Bai, H. Liu, R. Luo, A. Chen, and D. Li, *RSC Adv.* 4, 62862 (2014).

- 10.** Zhang, M. Cheng, G. Liu, Y. Gao, L. Zhao, S. Li, Y. Wang, F. Liu, X. Liang, T. Zhang, and G. Lu, *Sens. Actuators, B* 263, 387 (2018).
- 11.** Zhao, B. Huang, J. Zhou, and E. Xie, *Phys. Chem. Chem. Phys.* 16, 19327 (2014).
- 12.** J. Y. Kim, N. J. Choi, H. J. Park, J. Kim, D. S. Lee, and H. Song, *J. Phys. Chem. C* 118, 25994 (2014). 2
- 13.** J. Zhang, P. Tang, T. Liu, Y. Feng, C. Blackman, and D. Li, *J. Mater. Chem. A* 5, 10387 (2017).
- 14.** S.-Y. Jeong, J.-W. Yoon, T.-H. Kim, H.-M. Jeong, C.-S. Lee, Y. Chan Kang, and J.-H. Lee, *J. Mater. Chem. A* 5, 1446 (2017).
- 15.** Z. Zhang, Z. Wen, Z. Ye, and L. Zhu, *RSC Adv.* 5, 59976 (2015).
- 16.** J. Cao, Z. Wang, R. Wang, S. Liu, T. Fei, L. Wang, and T. Zhang, *RSC Adv.* 5, 36340 (2015).
- 17.** Wang, J. Deng, Z. Lou, and T. Zhang, *J. Mater. Chem. A* 2, 10022 (2014).